Biomaterials Science

ROYAL SOCIETY OF CHEMISTRY

PAPER

View Article Online
View Journal

Cite this: DOI: 10.1039/d2bm00424k

Polyphenol derived bioactive carbon quantum dot-incorporated multifunctional hydrogels as an oxidative stress attenuator for antiaging and *in vivo* wound-healing applications†

Md Moniruzzaman,‡[a] Sayan Deb Dutta,‡[b] Jin Hexiu,‡[c] Keya Ganguly,[b] Ki-Taek Lim *[b] and Jongsung Kim *[a]

Upregulation of certain enzymes, such as collagenase, tyrosinase, and elastase, is triggered by several extrinsic environmental factors, such as temperature, UV radiation, humidity, and stress, and leads to elasticity loss and skin pigmentation. Herein, dual-emissive polyaromatic carbon quantum dots (CQDs) with abundant phenolic moieties, that is green and yellow CQDs (G-CQDs and Y-CQDs, respectively), were prepared using a three-fold symmetric molecule, 1,3,5-trihydroxybenzene. The significant inhibition efficacy of the fabricated CQDs against collagenase, elastase, and tyrosinase, which play important roles in skin aging, revealed their excellent antiaging potential. Y-CQDs with large polyphenolic–polyaromatic domains and abundant –OH groups exhibited high enzyme inhibitory efficacy against skin aging, and their collagenase, elastase, and tyrosinase inhibitory efficacies were ~75 ± 4.2%, ~52 ± 3.1%, and ~35.3 ± 4.2%, respectively, at a concentration of 100 μg mL^{-1}. The most critical factor that delays wound healing is oxidative stress, which is caused by the overproduction of free radicals around inflamed tissue. CQDs were effective in suppressing UV-induced reactive oxygen species at the cellular level and improved the cell viability. Subsequently, CQD-incorporated dual-emissive biocompatible gelatin–methacryloyl hydrogels were constructed as wound dressing materials to promote wound healing *via* inducing the proliferation of fibroblasts, enhancing cell migration and alleviating inflammation and to provide antiaging benefits. Our results demonstrated that the fabricated CQDs with remarkable optical features, low cytotoxicity, and excellent antioxidant and antiaging properties can be used as bio-imaging probes, antiaging agents, and wound dressing materials for oxidative stress-related diseases in the nanomedicine and cosmetics industries.

Received 23rd March 2022,
Accepted 5th May 2022

DOI: 10.1039/d2bm00424k

rsc.li/biomaterials-science

1. Introduction

External environmental factors, such as UV radiation, mechanical stress, nicotine consumption, and weather change, and intrinsic factors, such as metabolic processes, hormones, and genetics, contribute to skin aging.[1] Specifically, reactive oxygen species (ROS) are produced upon overexposing skin to UV radiation, which damages cellular nutrients (carbohydrates, proteins, and lipids), resulting in physiological and morphological changes and premature photoaging.[2,3] Photoinduced ROS boost the production of matrix metalloproteinases (collagenase or elastase) in skin. The degradation of various extracellular matrix proteins, such as elastin or collagen, is caused by these enzymes and induces premature skin aging and loss of skin elasticity.[4] Moreover, long-term exposure to UV radiation promotes the activity of tyrosinase, which is a melanin-producing enzyme responsible for melanosis or brown skin spots.[5–7] UV-induced activation of collagenase, tyrosinase, and elastase is linked to various skin disorders, such as melanosis, elasticity loss, darkening, and wrinkle formation.

Numerous antiaging products containing ingredients such as hydroquinone, tretinoin, and tocopherol have been used to improve skin health.[8,9] However, the use of conventional antiaging products causes numerous side effects, such as skin irritation, burning, dryness, and erythema. In contrast, several plant-derived (*Eucalyptus camaldulensis*, *Eucalyptus globulus*,

[a]*Department of Chemical and Biological Engineering, Gachon University, 1342 Seongnam-daero, Seongnam-si, Gyeonggi-do 13120, Republic of Korea. E-mail: jongkim@gachon.ac.kr*
[b]*Department of Biosystems Engineering, Kangwon National University, Chuncheon-24341, Gangwon-do, Republic of Korea. E-mail: ktlim@kangwon.ac.kr*
[c]*Department of Plastic and Traumatic Surgery, Capital Medical University, Beijing-100069, Fengtai, China*

†Electronic supplementary information (ESI) available. See DOI: **https://doi.org/10.1039/d2bm00424k**

‡These authors contributed equally to this manuscript.

Eucalyptus rudis, and *Eucalyptus sinerea*) products, such as flavonoids, gallic acid, and galloyl derivatives, exhibit moderate antioxidant properties.[10] Furthermore, several polyphenol-rich herbal medications have been effective at treating age-related neurological complications.[11] However, excessive amounts of polyphenols can be harmful to the body.[12] Consequently, innovative nontoxic carbon-based nanomaterials with excellent antioxidant and antiaging activities that can be used at moderate doses should be developed.

There has been little progress in the exploration of the antiaging potential and wound-healing applications of polyphenolic CQDs. Wound healing involves an inflammatory phase to prevent wound infection.[13] However, to prevent infection, severe inflammation often develops around wounds, which can result in excessive production of ROS and oxidative stress.[14] *In vivo*, oxidative stress induces cellular damage and inhibits cell proliferation, resulting in prolonged healing or extensive damage to wound sites.[15] Consequently, using antioxidant wound dressing materials that can eliminate ROS is an effective method for promoting wound progression from the inflammatory to the cell proliferation stage, thereby accelerating healing.

CQDs have recently been explored as attractive nanomedicines with large-scale applications owing to their low cytotoxicity, remarkable chemical stability, facile and low-cost synthesis, excellent fluorescence, and high photostability.[16,17] CQDs have already been used in a variety of biomedical applications, such as drug delivery, photothermal therapy, photodynamic therapy, and combating microbial infections.[18] Conversely, hydrogels are three-dimensional (3D) porous structures comprising polymer matrices interconnected *via* physical or chemical crosslinks.[19] Hydrogels provide 3D support for cell growth and proliferation; therefore, they have been extensively used in traumatic wound dressing and tissue engineering because of their similarity to biological tissues.[20] Various biomaterials and nanoparticles have been used to promote wound healing and tissue repair. Carbon-based nanostructures, which include carbon nanotubes, graphene, and graphene-quantum-dot-incorporated hydrogels, have been recently used because of their biocompatibility.[21] In particular, zero-dimensional CQDs with unique tunable optical properties incorporated into polymeric hydrogels are remarkable platforms as multicolor 3D scaffolds for tissue regeneration and wound healing.[22,23] Among various hydrogels, gelatin–methacryloyl (GelMA) presents facile photoactive synthesis, remarkable mechanical properties, tailorable viscoelastic properties, and excellent therapeutic properties, such as antioxidant effects, in tissue repair.[24] Therefore, it is imperative to develop polyphenolic multicolor-emissive CQDs with excellent antioxidant and antiaging properties incorporated in a biocompatible GelMA hydrogel matrix for antiaging and wound healing applications.

In this study, dual-emissive polyaromatic CQDs with abundant phenolic moieties were prepared using 1,3,5-trihydroxybenzene. The fabricated bioactive CQDs demonstrated significant inhibition efficacy against collagenase, elastase, and tyrosinase, revealing their excellent antioxidant and antiaging potential. Subsequently, the dual-emissive CQDs were incorporated into a biocompatible GelMA hydrogel to construct a dual-emissive glowing wound dressing material for wound-healing applications. Scheme 1 presents the schematic for the synthesis of polyphenolic multifunctional GelMA-CQD hydrogels as a potential candidate for antiaging and *in vivo* wound-healing applications. Our results demonstrated that the fabricated CQDs with outstanding optical features, low cytotoxicity, and excellent antioxidant and antiaging properties can be used as bio-imaging probes, antiaging agents, and wound dressing materials for oxidative stress-related diseases in the nanomedicine and cosmetic industries.

2. Experimental

All the experimental procedures such as material synthesis, antioxidant activity, enzyme inhibition activity, cytotoxicity evaluation, and wound healing property have been detailed in the ESI.†

3. Results and discussion

3.1. Synthesis process of dual-emissive CQDs

We judiciously selected 1,3,5-trihydroxybenzene, a polyphenolic compound to fabricate CQDs with abundant phenolic moieties.[25] Multiple 1,3,5-trihydroxybenzene monomers underwent a six-membered ring cyclization by the removal of their

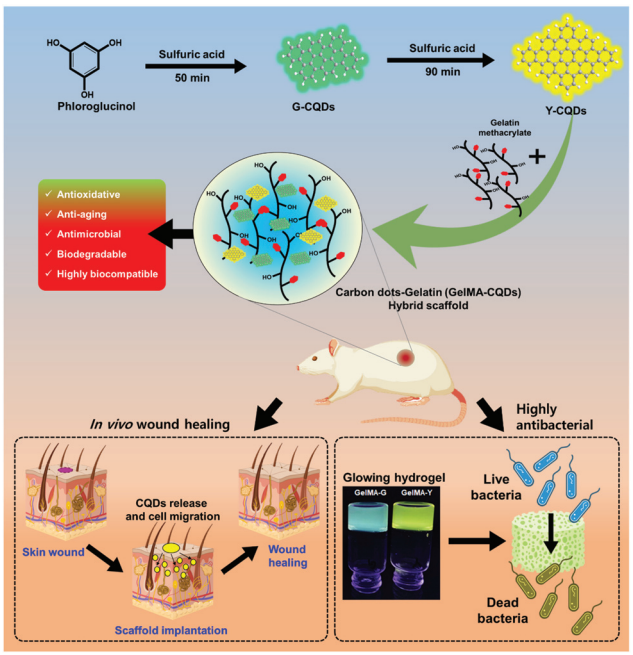

Scheme 1 Schematic for the synthesis process of polyphenolic multifunctional GelMA–CQD hydrogel as a potential candidate for antiaging and *in vivo* wound-healing applications.

–H and –OH moieties *via* a trimolecular reaction pathway and formed CQDs with polyaromatic structures in a dehydrating H_2SO_4 medium during a high-temperature process. The CQD formation process is shown in Fig. 1a. The evolution of the polyphenolic–polyaromatic CQD structure was examined using nuclear magnetic resonance (NMR) spectroscopy, and the results are shown in Fig. S2 (ESI†). The ^{1}H NMR spectra of the G- and Y-CQDs (Fig. S2b and c,† respectively) contained multiple new signals compared with the spectrum of the 1,3,5-trihydroxybenzene precursor (Fig. S2a†), owing to various proton environments. The spectrum of the precursor contained two primary peaks at ~5.8 and ~9.0 ppm, corresponding to different proton environments. In contrast, several polyaromatic proton signals emerged in the spectrum of the CQDs in the signal range of ~7.2–8.0 ppm, which revealed that multiple 1,3,5-trihydroxybenzene monomers fused to construct a polyaromatic CQD structure. Moreover, the multiple new signals in the range of 6.5–6.9 ppm were primarily attributed to the active protons of the –OH and sulfonic acid (–SO_3H) groups. Furthermore, several new signals, which were ascribed to different carbon environments, emerged in the ^{13}C NMR spectra of the G- and Y-CQDs (Fig. S2e and f,† respectively) compared with the spectrum of the precursor (Fig. S2d†). The ^{13}C NMR spectrum of the precursor contained two primary peaks at ~95 and ~159 ppm, corresponding to two different carbon environments (Fig. S2d†). In contrast, several polyaromatic carbon signals in the range of ~145–165 ppm was observed in the ^{13}C NMR spectra of the CQDs, indicating that multiple 1,3,5-trihydroxybenzene monomers were fused to construct large polyaromatic CQD structures featuring sp^2-carbon atoms and containing –OH groups at the edges. Moreover, unlike the ^{13}C NMR spectrum of 1,3,5-trihydroxybenzene, that of the CQDs included multiple peaks in the range of 115–140 ppm, indicating the development of intact sp^2 polyaromatic domains.

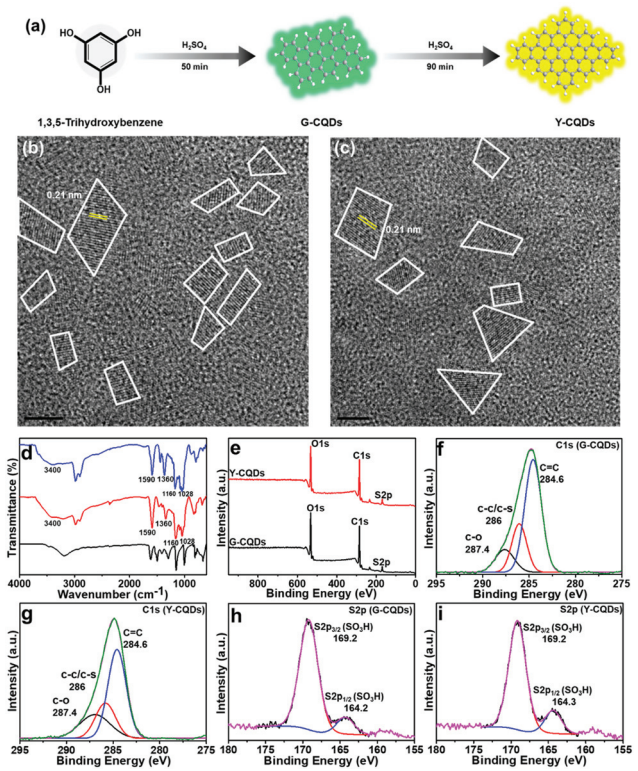

Fig. 1 Characterization of the dual-emissive CQDs. (a) Schematic of the plant-inspired dual-emissive CQDs synthesis process. HR-TEM images of the (b) G- and (c) Y-CQDs. Scale bars: 5 nm. (d) FT-IR spectra of 1,3,5-trihydroxybenzene and the G- and Y-CQDs. (e) XPS survey scan spectra and (f)–(i) high-resolution C 1s and S 2p XPS profiles of the G- and Y-CQDs.

3.2. Structural properties of the CQDs

Polyphenolic compounds with abundant surface –OH moieties are well known for their excellent antioxidant properties.[26] To develop CQDs with good antioxidant and antiaging properties, 1,3,5-trihydroxybenzene was used as the carbon precursor. The CQD formation process is illustrated in Fig. 1a. The high-resolution transmission electron microscopy (HR-TEM) images of the CQDs (Fig. 1b and c) revealed that the average sizes of the G-CQDs and Y-CQDs were ~4–7 nm and ~6–10 nm, respectively. Furthermore, the HR-TEM images revealed that the G- and Y-CQDs presented distinct lattice spacings of 0.21 nm (insets of Fig. 1b and c), indicating the interplanar separation of the (100) planes and confirming the defect-free structure of graphene.[25] X-ray diffraction (XRD, Smart Materials Research Center for IoT at Gachon University) and Raman spectroscopy experiments were performed to determine the phase composition and microstructures of the CQDs. The multiple crystalline peaks at ~16.9°, ~21.7°, ~23°, ~25.1°, ~27.2°, and ~28.1° in the XRD pattern of the precursor (Fig. S3a, ESI†) were converted into broad spectra upon thermal heating in the presence of H_2SO_4, thereby confirming the development of nanostructured conjugated polyaromatic CQDs.[27] The broad peaks at 23.4° and 22.4° in the XRD patterns of the G- and Y-CQDs, respectively, were ascribed to the (001) plane of graphene.[25] The diffraction peak of the Y-CQDs was narrower than that of the G-CQDs, suggesting that a longer thermal heating period led to the formation of larger particles with higher crystallinity.[17] In order to gain more insights into the relationship between the XRD spectra and the corresponding crystallite size of the particle, we have considered the Scherrer equation. The Scherrer equation is related to the average size of the crystalline or particle with peak broadening in a diffraction pattern in XRD spectra. Considering moderate crystalline nature as evident from HR-TEM and XRD, we used the Scherrer equation for the CQDs as follows.

$$\tau = \frac{K\lambda}{\beta \cos\theta} \quad (1)$$

where τ is the mean size of the crystallite domain or particle size or grain size. K is the dimensionless shape factor whose typical value is around 0.9. λ is X-ray wavelength (λ = 1.54 Å in

the case of CuKa1). β is the full width at half maxima of the XRD peak (value in radians). θ is the Bragg angle.

The FWHM was calculated by Gaussian fitting of XRD spectra as shown in Fig. S3b and c (ESI†). The average size of the crystallite or particles was calculated as given in Table S1 (ESI†). It is to be noted that G- and Y-CQDs exhibited an average crystallite size of the particle around 7.8 and 10 nm, respectively, which are well in accordance with the HR-TEM data. Moreover, the distinct shoulder peak at ~10° in the XRD pattern of the Y-CQDs was attributed to the significant aerial oxidation during the CQD growth in an open thermal heating system.[28] The Raman spectra of the CQDs (Fig. S3d, ESI†) were used to analyze the inherent nature of the CQDs, and the results revealed considerable graphitization during thermal heating.[29] The Raman spectra of the G- and Y-CQDs included two common peaks at ~1350 and ~1590 cm^{-1}, which correspond to the D- and G-bands, respectively. The D-band suggested the presence of a disordered carbon framework or surface defects owing to aerial oxidation. In contrast, the presence of the G-band implied the formation of sp^2-hybridized conjugated polyaromatic carbon networks because of the significant degree of graphitization achieved *via* dehydration-mediated condensation. The I_G/I_D ratios of the G- and Y-CQDs were greater than 1. This indicated the high quality of the graphene structure, which was also confirmed by the HR-TEM images.

The chemical composition and surface properties of the CQDs were examined by Fourier-transform infrared (FT-IR) spectroscopy and X-ray photoelectron spectroscopy (XPS). The G- and Y-CQDs comprised similar functional moieties or chemical bonds, as confirmed by their similar FT-IR spectra and XPS profiles. The FT-IR spectra of the G- and Y-CQDs (Fig. 1d) included the characteristic stretching vibrations of the C–O/C–S and O–H bonds at ~1160 and ~3400 cm^{-1}, respectively.[30] The stretching vibrational mode observed at ~1590 cm^{-1} was attributed to the C=C network of the carbon frameworks containing phenolic –OH groups at the zigzag edges.[31,32] The FT-IR spectra of both types of CQDs contained peaks at 1028 and 1360 cm^{-1}, which were attributed to the vibrational mode of the $-SO_3H$ groups.[33] Therefore, the FT-IR spectra indicated that the primary surface functional groups of both types of CQDs were –OH and $-SO_3H$. Furthermore, the elemental composition and valence states of the G- and Y-CQDs were analyzed using XPS. The C 1s, O 1s, and S 2p peaks in the XPS survey scan spectra of the G- and Y-CQDs (Fig. 1e) confirmed the presence of C, O, and S, respectively in the CQDs.[30] The high-resolution C 1s XPS profiles provided information on the elemental valence states and bonding nature of the CQDs. The C 1s XPS profiles of the G- and Y-CQDs (Fig. 1f and g, respectively) included three peaks at ~284.6, ~286 and ~287.4 eV, corresponding to the C=C, C–C/C–S, and C–O bonds, respectively. The integrated area of C–OH in the HR-XPS C 1s data has been calculated for G-, and Y-CQDs, and the ratio of the integrated area is as follows:

$$\frac{\text{Intergrated area of C} - \text{OH in C 1s (Y-CQDs)}}{\text{Intergrated area of C} - \text{OH in C 1s(G-CQDs)}} = 1.77$$

Thus, the ratio of the integrated area of C–OH in C 1s for Y-CQDs to G-CQDs is around 1.77, which suggests that Y-CQDs are composed of higher numbers of phenolic –OH groups on the surface, responsible for the enhanced antioxidant activity. The deconvoluted high-resolution S 2p XPS profiles of the G- and Y-CQDs (Fig. 1h and i, respectively) included two major peaks located at ~164.5 and 169.2 eV, which suggested the presence of the S $2p_{3/2}$ and S $2p_{1/2}$ of the $-SO_3H$ groups, respectively.[34] Therefore, the FT-IR spectroscopy and XPS data of the G- and Y-CQDs confirmed that the CQDs presented C=C, C–O, C–S, and $-C-SO_3H$ bonds or functional moieties. Moreover, to get more detailed information on the electrical potential on surface of the CQDs, zeta potential measurement was conducted as shown in Fig. S3e.† The zeta potential values (ξ) of G-, and Y-CQDs were −32.3 and 44.2 mV, respectively. The zeta potential values indicate that Y-CQDs probably contain higher numbers of negatively charged hydroxyl (–OH) functional moieties on the surface, resulting from the higher degree of polymerization of 1,3,5-trihydroxybenzene monomers, indicating a larger particle size.

3.3. Optical properties of the CQDs

UV–vis absorption spectroscopy was used to investigate the optical properties of the G- and Y-CQDs. The ethanolic dispersions of G- and Y-CQDs presented broad absorption bands at ~292 and ~307 nm, respectively, attributed to the π–π* transitions (Fig. 2a).[35,36] The precursor exhibited typical sharp absorption peak at 268 nm due to the π–π* transitions of the phenolic rings which was converted into a broad band in the absorption spectra of the CQDs.[37] The G-, and Y-CQDs presented a maximum PL emission intensity at 516 and 550 nm, respectively at the excitation of 345–350 nm. The inset of Fig. 2b shows corresponding green and yellow emission. The G- and Y-CQDs presented moderate excitation-dependent emission when excited at various wavelengths. The excitation-

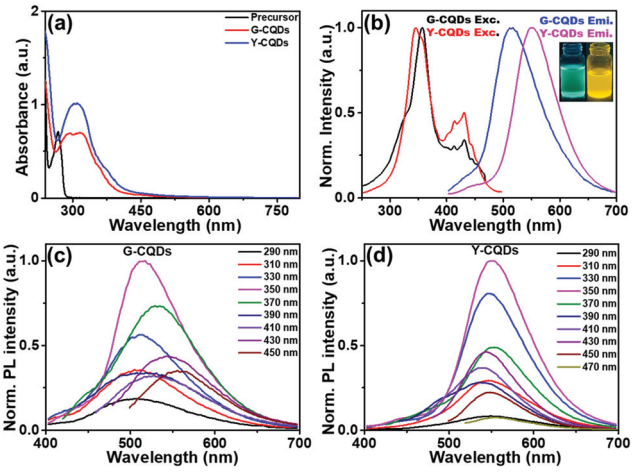

Fig. 2 Optical properties of the dual-emissive CQDs. (a) UV–vis absorption spectra of 1,3,5-trihydroxybenzene and the G- and Y-CQDs. (b) PL emission spectra of the G- and Y-CQDs. Excitation-dependent PL emission spectra of the (c) G- and (d) Y-CQDs.

dependent emission properties of the G- and Y-CQDs at excitation wavelengths in the range of 290–470 nm are presented in Fig. 2c and d, respectively.

3.4. *In vitro* antioxidant and antiaging properties of the polyphenolic CQDs

The inherent antioxidant and antiaging properties of the polyphenolic CQDs were investigated. To assess their antioxidant activities, a free radical scavenging assay was conducted as described in section 2.2 (ESI†) using 2,2-diphenyl-1-picrylhydrazyl (DPPH), and the results are presented in Fig. 3a. The G- and Y-CQDs presented higher radical scavenging ability than their precursor, which is a good antioxidant. Depending on the spectrophotometric changes arising from the reactions between DPPH$^{\bullet}$ and antioxidants, DPPH is often used to test the antioxidant properties of materials.[26] The free radical scavenging abilities of 1,3,5-trihydroxybenzene and the G- and Y-CQDs were compared with that of ascorbic acid (AA), which served as the positive control, at various concentrations. The Y-CQDs exhibited the highest free radical scavenging activity of 87.1 ± 3.6% at a concentration of 100 μg mL^{-1}, whereas the radical scavenging activity of the G-CQDs at the same concentration was 81.2 ± 3.5%. Furthermore, the radical scavenging activity of 1,3,5-trihydroxybenzene was only 64 ± 3.2% at a concentration of 100 μg mL^{-1}, which was significantly lower than that of the Y-CQDs. Moreover, the free radical scavenging activity of the Y-CQDs, was 68 ± 3.3% even at a low concentration of 30 μg mL^{-1}, which was superior to that of 1,3,5-trihydroxybenzene at a concentration of 100 μg mL^{-1}. The half-maximal inhibition effective concentration (EC_{50}) of the Y-CQDs was calculated to be 16 μg mL^{-1}, which was slightly higher than that of the standard antioxidant AA (EC_{50} = 10 μg mL^{-1}). The strong antioxidant activity of 1,3,5-trihydroxybenzene is ascribed to the reactions between its phenolic –OH moieties and free radicals *via* phenolic proton and electron donation, followed by resonance stabilization. The number of phenolic –OH moieties in polyphenols is directly related to the antioxidant activity of the polyphenols.[38] Therefore, the 1,3,5-trihydroxybenzene–derived polyphenolic CQDs with abundant phenolic –OH moieties exhibited excellent antioxidant properties even at low concentrations. The surface area of the Y-CQDs was significantly larger than that of the G-CQDs; therefore, the number of exposed phenolic –OH groups of the Y-CQDs was larger than that of the G-CQDs, accounting for the higher antioxidant activity of the Y-CQDs. Moreover, the antioxidant activity of the Y-CQDs was superior to that of the other literature-reported CQDs (Table 1).

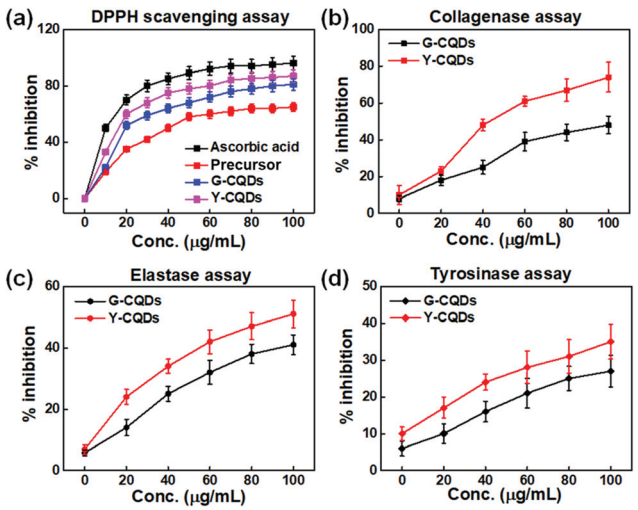

Fig. 3 *In vitro* antioxidant and antiaging properties of the CQDs. (a) DPPH radical scavenging assays of the G- and Y-CQDs in comparison with that of ascorbic acid as the control. (b) Collagenase, (c) elastase, and (d) tyrosinase inhibition assays using G- and Y-CQDs. Data are reported as means ± SDs of triplicate experiments.

Antioxidants can also reduce the concentration of free radicals in skin tissue, thereby inhibiting the expression of aging-related enzymes.[44] Therefore, to determine the suppressive efficacy of the CQDs, the concentrations of aging-related enzymes, that is collagenase, elastase, and tyrosinase, were measured according to the method described in sections 2.3.1 and 2.3.2 (ESI†). The collagenase inhibitory efficacy of the Y-CQDs was ~75 ± 4.2% at a concentration of 100 μg mL^{-1}, which was significantly higher than that of the G-CQDs (48 ± 3.2%) at the same concentration (Fig. 3b). Moreover, Y-CQDs with a concentration of 100 μg mL^{-1} exhibited anti-elastase and anti-tyrosinase activities, and their elastase suppression capability and tyrosinase inhibitory activity were 52 ± 3.1% (Fig. 3c) and 35.3 ± 4.2% (Fig. 3d), respectively. In previous studies, several types of nanoparticles have been used as aging-related enzyme inhibitors. For example, Radwan *et al.* reported that collagenase, elastase, and tyrosinase were effectively inhibited using silver nanoparticles derived from *Eucalyptus camaldulensis* bark extract with inhibitory efficacies of 63 ± 2.3%, 75.9 ± 6.8%, and 65 ± 5.87% at concentrations of

Table 1 Comparison table for antioxidant properties of CQDs

CQD precursor	Concentration (μg mL^{-1})	Radical scavenging activity (%)	Applications	Ref.
Salvia miltiorrhiza	200	88.9	ROS scavenging	39
Clove buds and polyvinylpyrrolidone	179	50	Antioxidant, catalysis, and bio-imaging	40
S,Se–CQDs	200	40	Antioxidant and bio-imaging	41
Date molasses	40	50	ROS scavenging	42
Garlic	80	50	ROS scavenging and cellular imaging	43
1,3,5-Trihydroxybenzene	100 (Y-CQDs)	87.1 ± 3.6	Antiaging and wound healing	This study

500, 300, and 500 μg mL^{-1}, respectively.[10] In addition, Shah *et al.*, reported that the inhibitory efficacies of *Silybum-marianum*-derived silver nanoparticles for collagenase, elastase, and tyrosinase were 23.7 ± 1.3%, 14.5 ± 1.1%, and 24.6 ± 1.6%, respectively.[45] Therefore, the as-prepared metal-free carbon-based Y-CQDs exhibited remarkable inhibitory efficacy toward the aging-related enzymes at low concentrations, rendering them excellent agents for cosmetic and nanomedicine applications.

Moreover, to assess the antioxidant potential of the CQDs at the cellular level, a fluorescence-based 2′,7′-dichlorofluorescin diacetate (DCF-DA) assay was performed on mesenchymal stem cells (hBMSCs) and human dermal fibroblasts (hDFs). DCF-DA is a cell-membrane-permeable probe often used to evaluate the production of ROS inside cells under stress conditions.[46] Although, typically, DCF-DA does not exhibit fluorescence, intracellular ROS can oxidize non-fluorescent DCF-DA to fluorescent DCF-DA inside cells under stress.[47] Therefore, the effect of the CQDs on the scavenging activity of intercellular ROS was determined by measuring the changes in the fluorescence intensity of hBMSCs under stress (UV irradiation) in the presence of different concentrations of CQDs. DCF-DA presented high intercellular fluorescence intensity after 10 min of UV irradiation in the absence of CQDs; furthermore, as the concentration of CQDs was increased, the fluorescence intensity decreased gradually (Fig. S4a, ESI†). These results indicated that under stress conditions (UV irradiation), the hBMSCs yielded abundant intercellular ROS, which were suppressed gradually by the increase in the CQD concentration. The Y-CQDs with superior antioxidant properties suppressed ~65% of the UV-induced ROS at the cellular level, compared with the G-CQDs, which suppressed only ~50% of the UV-induced ROS at the same concentration of 100 μg mL^{-1}. Moreover, the effect of the CQDs on the scavenging activity of H_2O_2-induced intercellular ROS in hDFs was measured by the fluorescence intensity of DCF-DA different CQD concentrations. The DCF-DA fluorescence intensity of hDFs upon H_2O_2 (100 μM) exposure in the presence of different concentrations of CQDs is presented in Fig. S4b (ESI†). The Y-CQDs with superior antioxidant properties suppressed ~68.8% of the H_2O_2-induced ROS at the cellular level, whereas the G-CQDs, suppressed only ~54% of the H_2O_2-induced ROS at the same concentration of 100 μg mL^{-1}. Therefore, the Y-CQDs outperformed the G-CQDs in suppressing the intercellular ROS produced in skin cells under external stress (photo or chemical).

The cytotoxic effects of the CQDs toward hBMSCs and hDFs were studied under external photo/chemical stress using different concentrations of CQDs and a standard WST-8 assay. The results were used to validate the potential applications of the CQDs as novel antiaging agents in the cosmetic and nanomedicine industries. Under identical experimental conditions, that is UV irradiation for 10 min, cell viability increased with increasing CQD concentration for both cell lines because of the increase in the UV-induced ROS suppression efficacies of the CQDs (Fig. S4c and d, ESI†). The Y-CQDs with superior antioxidant properties increased the viability of the hBMSCs by 39%, whereas the G-CQDs increased the viability of the hBMSCs by only ~26% at the same concentration of 100 μg mL^{-1}. Similarly, the Y-CQDs increased the viability of the hDFs subjected to UV irradiation for 10 min by 16.3%, whereas the G-CQDs increased the viability of the hDFs subjected to UV irradiation for 10 min by only 9.8% at the same concentration of 100 μg mL^{-1}. Moreover, the effect of CQD concentration on the viability of the H_2O_2-treated cells was measured, and the results showed a concentration-dependent increase in cell viability owing to the increase in the ROS suppressing efficacy of the CQDs (Fig. S4e and f, ESI†).

3.5. Preparation and characterization of the GelMA–CQDs composite hydrogels

Polyphenolic dual-emissive CQDs were incorporated into biocompatible GelMA hydrogel to obtain fluorescent dual-emissive GelMA–CQD hydrogels with antioxidant and antiaging properties for wound-healing applications. The CQDs were loaded into GelMA matrices, followed by photopolymerization using lithium phenyl-2,4,6-trimethylbenzoylphosphinate as the photoinitiator for 1 min to obtain UV-crosslinked gels. The synthesis of the GelMA–CQD hydrogels is described in section 2.4 (ESI†). The digital photographs of the GelMA–CQDs under visible and UV light illumination revealed that the CQDs retained their fluorescence after incorporation in the hydrogel frameworks (Fig. S5, ESI†).

The morphologies and functional groups of the freeze-dried hydrogel samples were analyzed using field-emission scanning electron microscopy (FE-SEM) and FT-IR spectroscopy. The FE-SEM images of the freeze-dried GelMA and GelMA–CQD composite hydrogels revealed their similar microporous morphologies and superior porosity of the GelMA–CQD composites (Fig. 4a). This indicated that the polyphenolic CQDs formed hydrogen bonds with the carboxylic acid groups of GelMA, leading to the formation of porous frameworks,

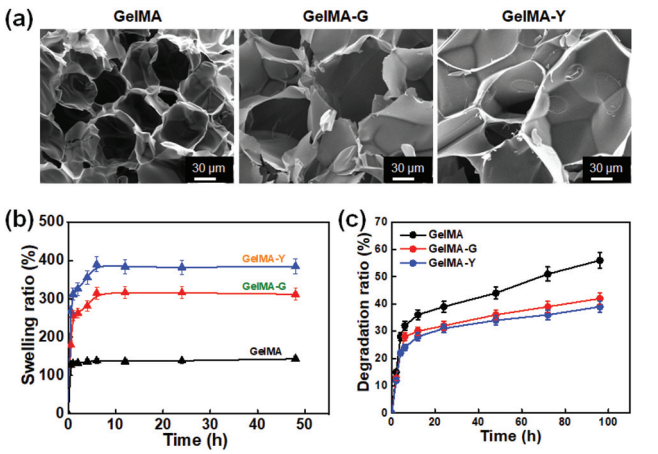

Fig. 4 Properties of the GelMA–CQD hydrogel scaffolds. (a) HR-SEM images of the pure GelMA, GelMA-G, and GelMA-Y scaffolds. Time evolution of the (b) swelling efficiencies and (c) degradation ratios of the fabricated scaffolds after immersion in PBS at ambient temperature.

which promoted CQD release according to bioenvironmental needs. The GelMA–CQD composites fabricated using the G- and Y-CQDs (GelMA-G and GelMA-Y, respectively) exhibited similar rough and flaky pure structures compared with that of the pure GelMA scaffold, which was consistent with previous reports.[48] The flaky and macroporous morphology of the GelMA scaffold can improve the swelling efficiency and facilitate fibroblast proliferation toward wound healing.[49–52] The peaks in the FT-IR spectra of the freeze-dried GelMA and GelMA-G and GelMA-Y composites were similar because of the low amounts of CQDs incorporated in the hydrogel matrices and lack of chemical interactions between the CQDs and the matrices (Fig. S6, ESI†). The peaks at ~3300 and ~1634 cm^{-1} corresponded to the stretching vibrations of the –OH and –C═O functional groups, respectively.[53] The peak at 1549 cm^{-1} in the FT-IR spectrum of pure GelMA, which corresponded to the amide –N–H bonds, was slightly shifted toward 1524 cm^{-1} in the spectrum of the GelMA–CQDs, suggesting the formation of hydrogen bonds between the –OH groups of the CQDs and –N–H groups of GelMA.

Subsequently, the swelling and degradation behavior of each GelMA–CQD composite were investigated in the presence of phosphate-buffered saline (PBS) according to method described in section 2.5 (ESI†). Swelling behavior is one of the most critical features of hydrogel composites used for biomedical applications. Swelling performance is strongly related to the rehydration potential and durability of natural structures, and indirectly reveals the structural properties and mechanical stiffness of structures.[49] The swelling of the freeze-dried GelMA scaffold, which effectively preserves the moisture of the surroundings, was favorable for wound healing.[54] The swelling efficacies of GelMA and the GelMA–CQDs were tested in PBS buffer at 37 °C, and the results are presented in Fig. 4b. The swelling abilities of the GelMA–CQD composite hydrogels were higher than that of bare GelMA, as expected. The presence of hydrophilic –OH groups, extent of crosslinking, and amorphous and/or crystalline nature significantly affect the swelling potential of hydrogels.[55] The swelling efficiencies of the GelMA-G and GelMA-Y composite hydrogels (~300% and ~400%, respectively) were significantly higher than that of the pure GelMA scaffold (~150%) after 50 h of incubation (Fig. 4b). The superior swelling potential of the GelMA–CQD composite hydrogels compared with that of the bare GelMA was attributed to the larger pores and abundant phenolic –OH groups of the polyphenolic CQDs in the GelMA–CQD composite hydrogels, which promoted the formation of hydrogen bonds between the CQDs and GelMA scaffold. The number of available hydrophilic –OH groups of the Y-CQDs was higher than that of the G-CQDs; therefore, the water absorption capacity of the GelMA-Y composite hydrogel was higher than that of the GelMA-G composite hydrogel. Furthermore, the swelling behavior, expansion ratio, and solid properties of the GelMA-Y composite hydrogel were superior to those of the GelMA-G composite hydrogel.[55] Furthermore, the degradation ratios of the fabricated composite hydrogels were determined in PBS at ambient temperature (Fig. 4c). After 4–5 h, the scaffolds reached the saturation swelling point and became semi-transparent hydrogels. Likewise, the strong interaction between GelMA and CQDs not only enhanced the swelling efficiency but also decreased the degradation rate compared to

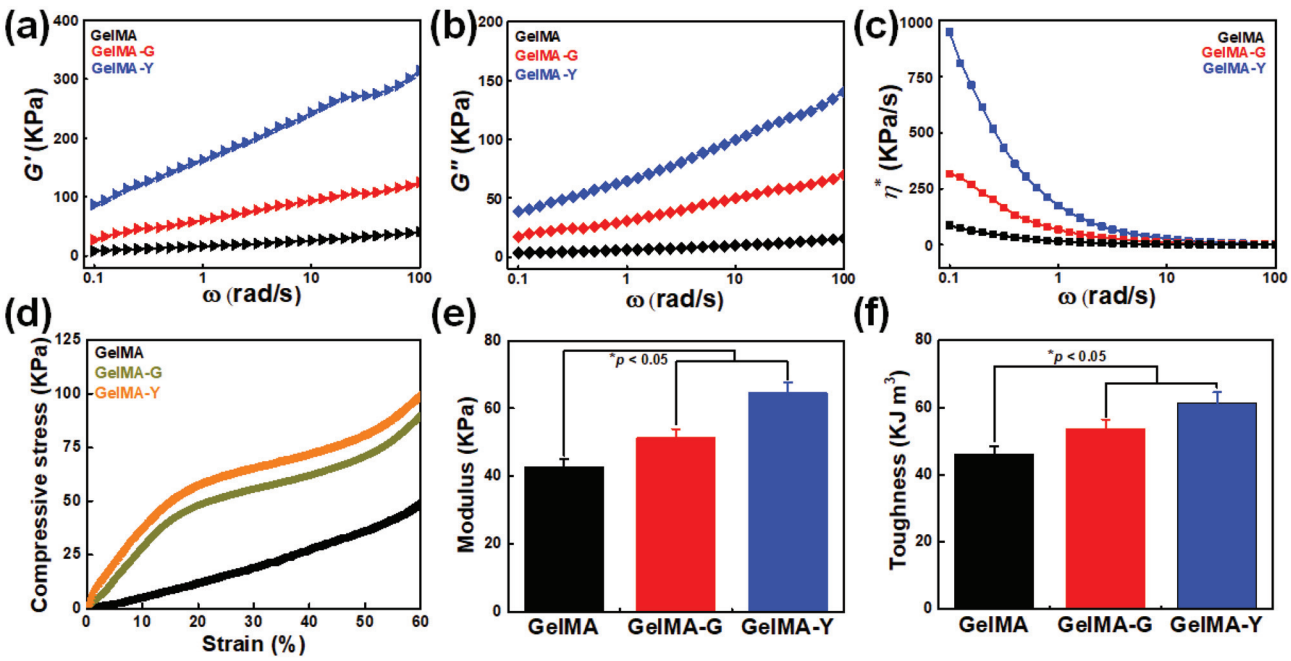

Fig. 5 Rheological and mechanical behaviors of the developed scaffolds. (a) Storage moduli (G'), (b) loss moduli (G'') and (c) complex viscosities (η^*) of the hydrogels at ambient temperature in the shear rate range of 0.1–100 rad s^{-1}. (d) Compressive stress–strain curves, (e) compressive moduli, and (f) toughness of the as-prepared hydrogels at ambient temperature.

pure GelMA scaffolds (Fig. 4c). Therefore, we anticipated that the developed GelMA–CQD composite hydrogels presented excellent swelling efficacy and low degradability, rendering them useful as ideal wound dressing materials for promoting hydration/dehydration in the wound bed.[56]

3.6. Rheological and mechanical properties of the GelMA–CQDs composite hydrogels

The mechanical strength (storage modulus (G'), loss modulus (G''), and complex viscosity (η^*)) of the hydrogel composites was investigated using a rotational rheometer at ambient temperature in the angular frequency range of 0.1–100 rad s^{-1}, and the results are shown in Fig. 5. The G', G'' and η^* values of pure GelMA and the GelMA–CQD composite hydrogels were evaluated. The G' and G'' values of the GelMA–CQDs samples increased at higher rates than those of pure GelMA (Fig. 5a and b). The G′ values of the GelMA-G and GelMA-Y composite hydrogels at 100 rad s^{-1} were higher than that of pure GelMA. Moreover, the η^* values of the GelMA-G and GelMA-Y composite hydrogels at 0.1 rad s^{-1} were 300 and 1000 kPa s^{-1}, respectively (Fig. 5c). These values were significantly higher than that of pure GelMA (65 kPa s^{-1}) and indicated the good shear-thinning nature of the GelMA–CQD composite hydrogels.[48,57,58] As the shear rate was increased from 0.1 to 100 rad s^{-1}, the η^* values of all the hydrogel samples decreased considerably. To evaluate the mechanical properties of the developed scaffolds, we performed compression experiments using a universal compression testing machine (A & D Digital,

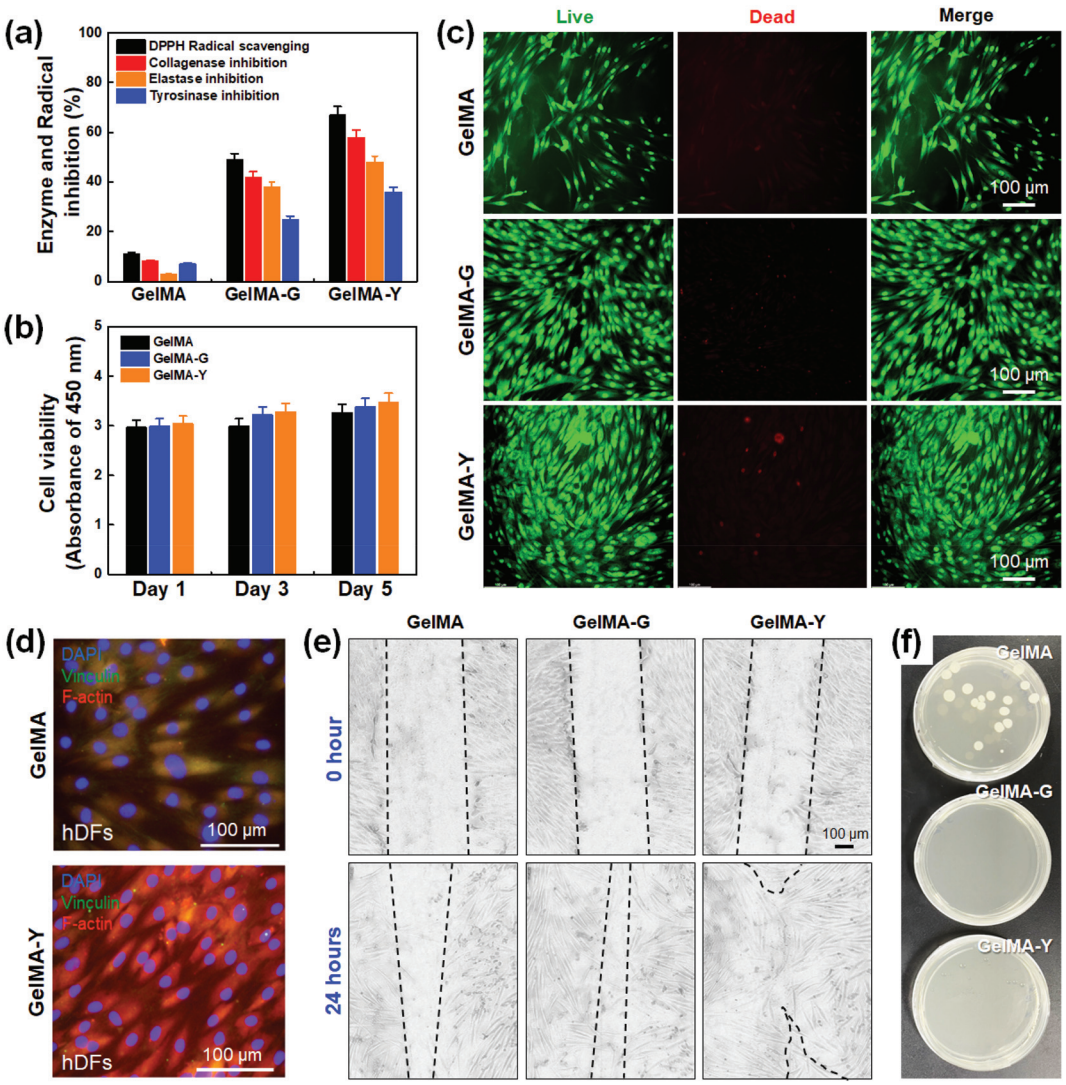

Fig. 6 *In vitro* bioactivity of the GelMA–CQDs hydrogels. (a) DPPH and enzyme inhibitory assays of the developed GelMA–CQD hydrogels. (b) Cytotoxicity evaluation of the GelMA–CQD hydrogels on hDFs after 3 d of incubation. (c) Representative live/dead assays of the hDFs incubated with the hydrogels after 3 d of treatment. (d) Evaluation of the cytoskeletal protein (vinculin and F-actin) expression in the presence of the GelMA and GelMA-Y hydrogels after 3 d of incubation. (e) Representative bright field images of the hDFs in the wound healing assay at 0 and 24 h. (f) Digital photographs of the agar plates showing the antibacterial efficacy of the developed hydrogels against *Bacillus subtilis*. Data are reported as means ± SDs of triplicate experiments, statistical significance at $*p < 0.05$.

Japan). The compressive stresses of the GelMA–CQDs scaffolds were higher than that of the pure GelMA scaffold (Fig. 5d). Moreover, the compressive moduli of the GelMA-G and GelMA-Y scaffolds were slightly higher than that of pure GelMA, suggesting that the CQDs improved the mechanical support properties of the GelMA scaffolds (Fig. 5e). Furthermore, the toughnesses of the GelMA, GelMA-G, and GelMA-Y scaffolds were calculated to be 48.25, 58.47, and 62.54 kJ m^{-3}, respectively (Fig. 5f). These results suggested that the developed composite hydrogel scaffolds were mechanically strong, and the mechanical stiffness of the GelMA–CQD scaffolds was improved by the incorporation of the CQDs, rendering the GelMA–CQD scaffolds useful for developing skin grafts for wound-healing applications.

3.7. *In vitro* bioactivity and wound-healing properties of the GelMA–CQD hydrogels

The antioxidant and antiaging properties of the GelMA, GelMA-G, and GelMA-Y hydrogels were investigated according to the procedure mentioned in section 2.6 (ESI†), and the results are shown in Fig. 6a. GelMA-Y exhibited the highest radical scavenging activity of 67.1 ± 3.1% at a concentration of 100 μg mL^{-1}, whereas the radical scavenging activity of the GelMA-G was only 49 ± 2.7% at the same concentration. Moreover, the suppressive efficacies of the GelMA–CQD composite hydrogels on the aging-related enzymes, that is collagenase, elastase, and tyrosinase, were measured. The collagenase, elastase, and tyrosinase inhibitory efficacies of the GelMA-Y composite hydrogel reached ~58 ± 2.8%, ~48 ± 2.3%, and ~36 ± 1.8%, respectively, at a concentration of 100 μg, mL^{-1}, whereas the collagenase, elastase, and tyrosinase inhibitory efficacies of the GelMA-G were only 42 ± 2.1%, 38 ± 1.8%, and 25 ± 1.3%, respectively, at the same concentration. The radical scavenging and enzyme inhibitory activity of the GelMA hydrogel matrix, which was used as the control, were negligible compared with those of the GelMA–CQD composite hydrogels. The DPPH radical scavenging and aging-related enzyme inhibitory activities of the GelMA–CQD composite hydrogels were lower than those of the corresponding pure CQDs because of the limited release of hydrogel-bound CQDs; however, the

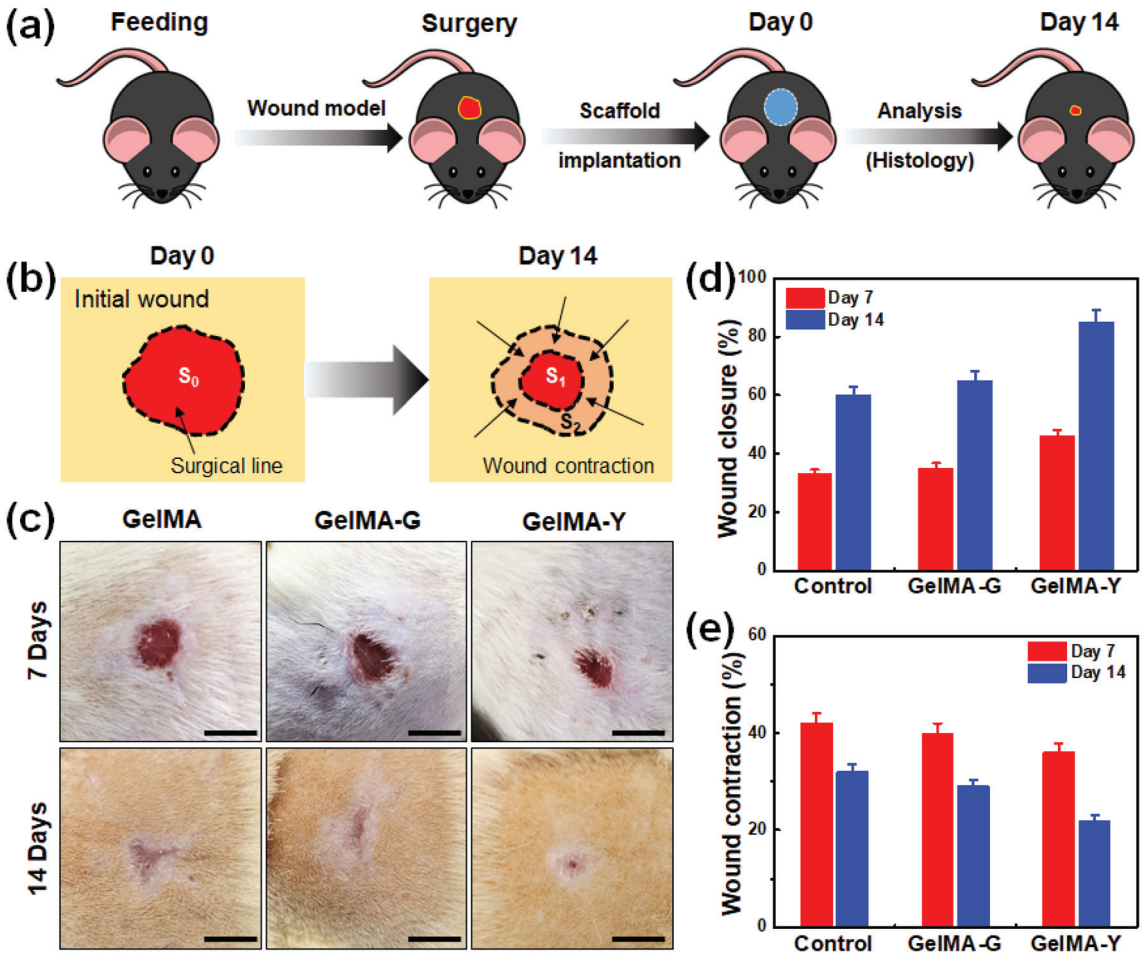

Fig. 7 Macroscopic *in vivo* wound healing efficacy of the developed hydrogel scaffolds. (a) Schematic of the timeline of the *in vivo* experiments. (b) Schematic of the wound closure and contraction evolution. (c) Digital photographs of the rats (n = 3) after 7 and 14 d of wound healing test. Scale bars: 10 mm. (d) and (e) Quantitative evaluation of the macroscopic wound closures and contractions. Data are reported as means ± SDs of triplicate experiments, statistical significance at $*p < 0.05$.

effectiveness of the GelMA–CQD composite hydrogels was suitable for practical applications.

The *in vitro* cytotoxicity of the fabricated hydrogels toward hDFs was evaluated using WST-8 assays, and the results are shown in Fig. 6b. The GelMA, GelMA-G, and GelMA-Y hydrogels were nontoxic toward hDFs, suggesting the biocompatibility of the CQDs at a concentration of 100 μg mL^{-1}. The viability of the hDFs exposed to the GelMA-Y hydrogel was the highest after 5 d of incubation. To confirm the biocompatibility of the GelMA–CQD hydrogels, we performed a live/dead hDF assay after 3 d of culture. The percentage of live cells in the presence of the GelMA-G and GelMA-Y composite hydrogels (≥95%) were significantly higher than those in the presence of pure GelMA (Fig. 6c). The fluorescence microscopy images of hDFs stained with vinculin and F-actin probes after 3 d of culture are presented in Fig. 6d. The number of densely packed cells in the presence of the GelMA-Y composite hydrogel was higher than that in the presence of the pure GelMA hydrogel. The morphology and cytoskeletal protein expression of the hDFs exposed to the GelMA-Y composite hydrogel were comparable to those of the untreated hDFs. These results suggested that the fabricated GelMA–CQD composite hydrogels were highly biocompatible owing to their excellent antioxidative and antiaging properties.[22]

Next, we investigated the *in vitro* wound-healing efficacy of the developed hydrogels using a scratch healing assay. A scaffold-leaching medium was prepared after incubating the freeze-dried scaffolds and culturing with wounded hDFs for 24 h. The photographs taken after incubation using a complementary metal–oxide-semiconductor camera were used to evaluate the wound-healing activities of the hydrogels, and the results are presented in Fig. 6e. The wound and hDF healing capacities of the GelMA-G and GelMA-Y scaffold hydrogels were superior to those of pure GelMA. The relative wound area in the presence of the GelMA-Y scaffold was significantly lower than that of the other groups, further demonstrating the excellent bioactivity of the Y-CQDs (Fig. S7, ESI†). Polyphenols are well known for their excellent antibacterial properties; therefore, we investigated the antibacterial properties of the GelMA–CQD hydrogels against *Bacillus subtilis*.[59–61] The GelMA–CQD

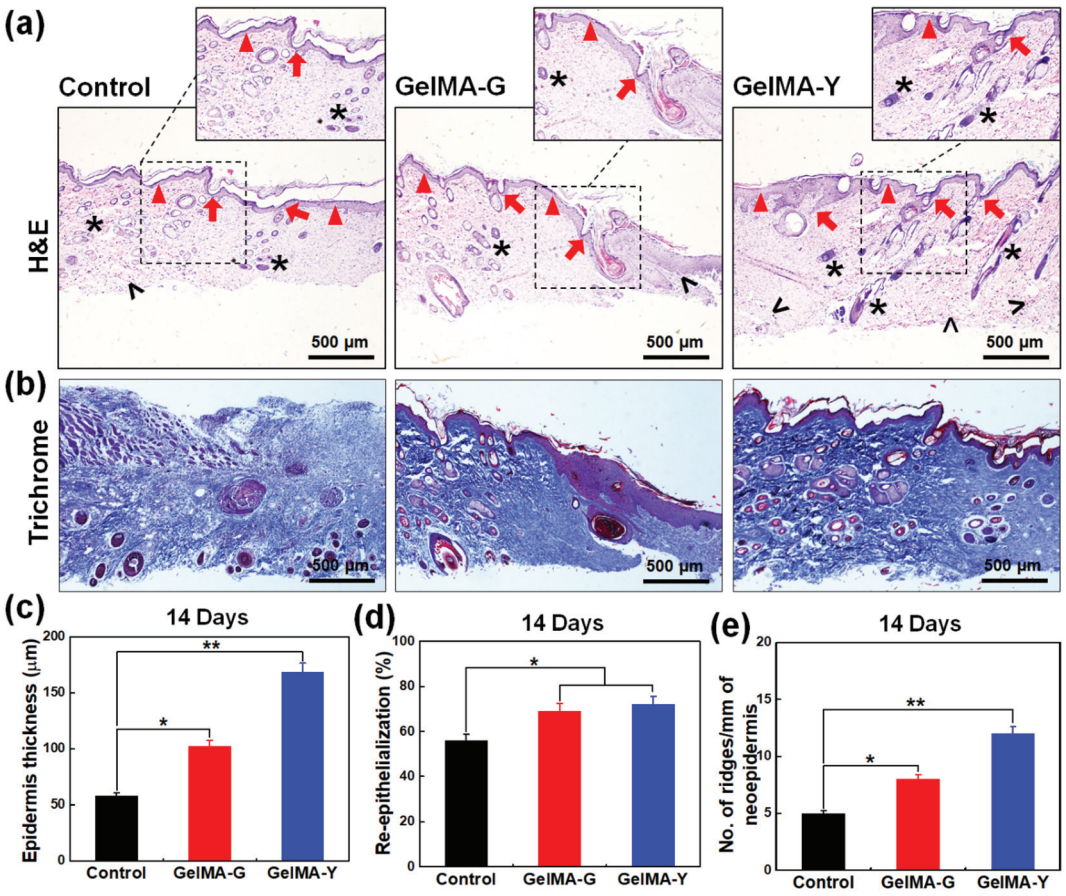

Fig. 8 Microscopic evaluation of *in vivo* wound healing. (a) Representative H&E staining images of the wound bed 14 d post-implantation. The black arrows, red triangles, red arrows, and black arrowheads indicate the formation of sebaceous glands, epidermis, hair follicles or epidermal ridges, and blood vessels, respectively. The boxed-areas represent magnified images of the histological sections. (b) Representative Masson trichrome stained images of wound tissue 14 d post-implantation illustrating collagen deposition. Quantitative evaluation of the (c) epidermal thickness, (d) skin re-epithelialization, and (e) neoepidermal ridges after 14 d of treatment. Data are reported as means ± SDs of triplicate experiments, statistical significance at $*p < 0.05$ and $**p < 0.01$.

treatment significantly inhibited bacterial colony formation after 24 h of incubation compared with pure GelMA (Fig. 6f). These results suggested that the GelMA–CQD hydrogels were highly biocompatible with strong antibacterial properties and can be used as multifunctional wound dressing materials for skin injuries.

3.8. Wound-healing properties of the GelMA–CQD scaffolds in a rat model

To evaluate the *in vivo* wound-healing efficacy of the developed GelMA–CQD hydrogel scaffolds, we used a subcutaneous wound model. The *in vivo* wound-healing experiments on rat model has been described in section 2.7 (ESI†). Fig. 7a shows the steps of the *in vivo* animal tests in this study. The rats were randomly divided into three groups: (i) pure GelMA (control group), (ii) GelMA-G (treatment group 1), and (iii) GelMA-Y (treatment group 2). All the scaffolds were sterilized using UV irradiation, followed by washing with 70% ethanol prior to implantation. The macroscopic wound closures were evaluated 7 and 14 d after scaffold implantation, and the wound closure and contraction are illustrated in Fig. 7b. Because we used healthy rats for this test, the wounds in all the experimental groups closed. However, the wound-healing rate of the GelMA-Y-treated rats (~85%) was significantly higher than those of the GelMA-G-treated rats (~65%) and GelMA-treated rats (~60%) after 14 d (Fig. 7c). The percentage of macroscopic wound closure ($S_0/S_1 \times 100$) and wound contraction ($S_0 - S_2/S_1 \times 100$) after 7 and 14 d of scaffold implantation are shown in Fig. 7d and e, respectively. To confirm macroscopic wound healing, the wounds, which were stained with hematoxylin and eosin (H&E) and Masson's trichrome 14 d post-implantation, were observed under a microscope. The H&E staining images of the wound bed and corresponding quantitative characterizations are presented in Fig. 8a. The formation of collagen and connective tissue was investigated using trichrome staining, and the results are illustrated in Fig. 8b. A thicker epidermis formation was observed in the presence of the GelMA-Y scaffold than in the other treatment groups, indicating the completion of the healing process (Fig. 8c). Furthermore, higher levels of wound re-epithelialization and granulation were observed in the presence of the GelMA-Y scaffold after 14 d of implantation (Fig. 8d). CQD-loaded scaffolds have been previously demonstrated to improve wound healing by inducing fibroblast proliferation and enhancing cell migration toward the wound bed.[22,62] Over time, the migration of skin cells, macrophages, and endothelial cells in the wounded area was enhanced to provide growth factors and promote the formation of the skin extracellular matrix.[22,63,64] Blood vessel formation was also observed in all the groups and was the most prominent in the GelMA-Y groups, suggesting that the CQDs played a critical role in neoangiogenesis during wound healing. The number of epidermal ridges and hair follicles, which are indicators of wound healing completion, in the GelMA-Y-treated group were the highest among all groups (Fig. 8e). Moreover, no inflammation was observed in all the treated samples, indicating the biocompatibility of the developed scaffolds. Therefore, we concluded that the GelMA–CQD hydrogels were highly antimicrobial, promoted *in vivo* wound healing, and could be used as smart nanomaterials for treating skin injuries.

4. Conclusion

In this study, dual-emissive polyaromatic CQDs with abundant phenolic moieties were prepared using a three-fold symmetric molecule, 1,3,5-trihydroxybenzene. The CQDs exhibited excellent antioxidant properties and significant inhibition efficacy against skin-aging-related enzymes, namely collagenase, elastase, and tyrosinase, indicating their excellent antiaging potential. Y-CQDs with large polyphenolic–polyaromatic domains and abundant –OH moieties exhibited the highest enzyme inhibitory efficacy against skin aging, and their collagenase, elastase, and tyrosinase inhibitory efficacies were ~75 ± 4.2%, ~52 ± 3.1%, and ~35.3 ± 4.2%, respectively, at a concentration of 100 μg mL^{-1}. The CQDs were effective at suppressing UV-induced ROS at the cellular level and improving cell viability. Subsequently, CQD incorporated dual-emissive biocompatible gelatin–methacryloyl hydrogels were constructed as wound dressing materials to promote wound healing *via* inducing the proliferation of fibroblasts, enhancing cell migration and alleviating inflammation, and to provide antiaging benefits. Our results demonstrated that the CQDs with remarkable optical features, low cytotoxicity, and excellent antioxidant and antiaging properties can be used as bio-imaging probes, antiaging agents, and wound dressing materials for oxidative-stress related diseases in the nanomedicine and cosmetics industries.

Conflicts of interest

There are no conflicts to declare.

Acknowledgements

This research was supported by the Basic Science Research Program through the National Research Foundation of Korea (NRF) funded by the Ministry of Education (Grant No. 2021R1A6A1A03038996). This study was also supported by the Basic Science Research Program through the National Research Foundation of Korea (NRF) funded by the Ministry of Education (No. 2018R1A6A1A03025582 & 2019R1D1A3A03103828), Republic of Korea. This work was also supported by the grants received from the National Natural Science Foundation of China (Grant No. 81700926) and Beijing Hospitals Authority Youth Program (Grant No. QML2019503). We thank the Smart Materials Research Center for IoT at Gachon University for their technical support with instruments (FT-IR and UV–Vis spectroscopy). All the surgical procedures were approved by the Animal Ethical and Approval Committee (AEAC) of the

Capital Medical University, Beijing, China (Permission No. KQYY-202012-004).

References

1 L. Rittié and G. J. Fisher, *Ageing Res. Rev.*, 2002, **1**, 705–720.
2 S. Pillai, C. Oresajo and J. Hayward, *Int. J. Cosmet. Sci.*, 2005, **27**, 17–34.
3 R. Pandel, B. Poljšak, A. Godic and R. Dahmane, *ISRN Dermatol.*, 2013, **2013**, 1–11.
4 P. Pittayapruek, J. Meephansan, O. Prapapan, M. Komine and M. Ohtsuki, *Int. J. Mol. Sci.*, 2016, **17**, 868.
5 J. W. Liu, Y. M. Wang, L. Xu, L. Y. Duan, H. Tang, R. Q. Yu and J. H. Jiang, *Anal. Chem.*, 2016, **88**, 8355–8358.
6 C. A. Ferguson and S. H. Kidson, *Pigm. Cell Res.*, 1997, **10**, 127–138.
7 Y. Hua, C. Ma, T. Wei, L. Zhang and J. Shen, *Int. J. Mol. Sci.*, 2020, **21**, 313.
8 M. Keen and I. Hassan, *Indian Dermatol. Online J.*, 2016, **7**, 311.
9 S. Mukherjee, A. Date, V. Patravale, H. C. Korting, A. Roeder and G. Weindl, *Clin. Interventions Aging*, 2006, **1**, 327–348.
10 R. A. Radwan, Y. A. El-Sherif and M. M. Salama, *Colloids Surf., B*, 2020, **191**, 111004.
11 J. Luo, H. Si, Z. Jia and D. Liu, *Antioxidants*, 2021, **10**, 1–20.
12 J. Yeo, J. Lee, S. Yoon and W. J. Kim, *Biomater. Sci.*, 2020, **8**, 1148–1159.
13 K. A. Bielefeld, S. Amini-Nik and B. A. Alman, *Cell. Mol. Life Sci.*, 2013, **70**, 2059–2081.
14 C. M. Sims, S. K. Hanna, D. A. Heller, C. P. Horoszko, M. E. Johnson, A. R. Montoro Bustos, V. Reipa, K. R. Riley and B. C. Nelson, *Nanoscale*, 2017, **9**, 15226–15251.
15 M. Zhang, X. Zhai, T. Ma, Y. Huang, C. Yan and Y. Du, *Chem. Eng. J.*, 2021, **423**, 130301.
16 S. Bayda, E. Amadio, S. Cailotto, Y. Frión-Herrera, A. Perosa and F. Rizzolio, *Nanoscale Adv.*, 2021, **3**, 5183–5221.
17 M. Moniruzzaman, B. Anantha Lakshmi, S. Kim and J. Kim, *Nanoscale*, 2020, **12**, 11947–11959.
18 B. Geng, D. Yang, D. Pan, L. Wang, F. Zheng, W. Shen, C. Zhang and X. Li, *Carbon*, 2018, **134**, 153–162.
19 J. Qu, X. Zhao, Y. Liang, T. Zhang, P. X. Ma and B. Guo, *Biomaterials*, 2018, **183**, 185–199.
20 H. Yuk, B. Lu and X. Zhao, *Chem. Soc. Rev.*, 2019, **48**, 1642–1667.
21 A. K. Gaharwar, N. A. Peppas and A. Khademhosseini, *Biotechnol. Bioeng.*, 2014, **111**, 441–453.
22 F. Cui, J. Sun, J. Ji, X. Yang, K. Wei, H. Xu, Q. Gu, Y. Zhang and X. Sun, *J. Hazard. Mater.*, 2021, **406**, 124330.
23 M. Omidi, A. Yadegari and L. Tayebi, *RSC Adv.*, 2017, **7**, 10638–10649.
24 A. G. Kurian, R. K. Singh, K. D. Patel, J. H. Lee and H. W. Kim, *Bioact. Mater.*, 2022, **8**, 267–295.
25 F. Yuan, T. Yuan, L. Sui, Z. Wang, Z. Xi, Y. Li, X. Li, L. Fan, Z. Tan, A. Chen, M. Jin and S. Yang, *Nat. Commun.*, 2018, **9**, 1–11.
26 M. H. Son, S. W. Park and Y. K. Jung, *Nanotechnology*, 2021, **32**, 415102.
27 P. Kumar, S. Senthamilselvi and M. Govindaraju, *RSC Adv.*, 2014, **4**, 26787–26795.
28 M. Moniruzzaman and J. Kim, *Appl. Surf. Sci.*, 2021, **552**, 149372.
29 A. Beda, P. L. Taberna, P. Simon and C. Matei Ghimbeu, *Carbon*, 2018, **139**, 248–257.
30 G. Yang, X. Wan, Y. Su, X. Zeng and J. Tang, *J. Mater. Chem. A*, 2016, **4**, 12841–12849.
31 C. S. Estes, A. Y. Gerard, J. D. Godward, S. B. Hayes, S. H. Liles, J. L. Shelton, T. S. Stewart, R. I. Webster and H. F. Webster, *Carbon*, 2019, **142**, 547–557.
32 E. Fuente, J. A. Menéndez, M. A. Díez, D. Suárez and M. A. Montes-Morán, *J. Phys. Chem. B*, 2003, **107**, 6350–6359.
33 S. Suganuma, K. Nakajima, M. Kitano, D. Yamaguchi, H. Kato, S. Hayashi and M. Hara, *J. Am. Chem. Soc.*, 2008, **130**, 12787–12793.
34 A. Shukla, S. D. Bhat and V. K. Pillai, *J. Membr. Sci.*, 2016, **520**, 657–670.
35 M. Sudolská, M. Dubecký, S. Sarkar, C. J. Reckmeier, R. Zbořil, A. L. Rogach and M. Otyepka, *J. Phys. Chem. C*, 2015, **119**, 13369–13373.
36 A. Sharma, T. Gadly, S. Neogy, S. K. Ghosh and M. Kumbhakar, *J. Phys. Chem. Lett.*, 2017, **8**, 1044–1052.
37 D. Zhang, C. Wang, L. Shen, H. C. Shin, K. B. Lee and B. Ji, *RSC Adv.*, 2018, **8**, 1963–1972.
38 J. Chen, J. Yang, L. Ma, J. Li, N. Shahzad and C. K. Kim, *Sci. Rep.*, 2020, **10**, 1–9.
39 Y. Li, W. Li, X. Yang, Y. Kang, H. Zhang, Y. Liu and B. Lei, *ACS Appl. Nano Mater.*, 2021, **4**, 113–120.
40 A. Kumar, K. Bankoti, T. Kumar and S. Dhara, *Hydrothermal Synthesis of Clove Bud-Derived Multifunctional Carbon Dots Passivated with PVP-Antioxidant, Catalysis, and School of Nano Science and Technology*, Indian Institute of Technology Kharagpur, School of Medical Science and Technology, Indian, 2022.
41 G. Huang, Y. Lin, L. Zhang, Z. Yan, Y. Wang and Y. Liu, *Sci. Rep.*, 2019, **9**, 1–9.
42 B. Das, P. Dadhich, P. Pal, P. K. Srivas, K. Bankoti and S. Dhara, *J. Mater. Chem. B*, 2014, **2**, 6839–6847.
43 S. Zhao, M. Lan, X. Zhu, H. Xue, T. W. Ng, X. Meng, C. S. Lee, P. Wang and W. Zhang, *ACS Appl. Mater. Interfaces*, 2015, **7**, 17054–17060.
44 R. Ganceviciene, A. I. Liakou, A. Theodoridis, E. Makrantonaki and C. C. Zouboulis, *Dermatoendocrinology*, 2012, **4**, 308–319.
45 M. Shah, S. Nawaz, H. Jan, N. Uddin, A. Ali, S. Anjum, N. Giglioli-Guivarc'h, C. Hano and B. H. Abbasi, *Mater. Sci. Eng., C*, 2020, **112**, 110889.
46 H. K. Kim, *Nutr. Res. Pract.*, 2016, **10**, 371–376.
47 W. H. Chan, C. C. Wu and J. S. Yu, *J. Cell. Biochem.*, 2003, **90**, 327–338.
48 B. Geng, F. Fang, P. Li, S. Xu, D. Pan, Y. Zhang and L. Shen, *Chem. Eng. J.*, 2021, **417**, 128125.

49 W. Xu, B. Z. Molino, F. Cheng, P. J. Molino, Z. Yue, D. Su, X. Wang, S. Willför, C. Xu and G. G. Wallace, *ACS Appl. Mater. Interfaces*, 2019, **11**, 8838–8848.
50 N. Zandi, B. Dolatyar, R. Lotfi, Y. Shallageh, M. A. Shokrgozar, E. Tamjid, N. Annabi and A. Simchi, *Acta Biomater.*, 2021, **124**, 191–204.
51 N. Annabi, D. Rana, E. Shirzaei Sani, R. Portillo-Lara, J. L. Gifford, M. M. Fares, S. M. Mithieux and A. S. Weiss, *Biomaterials*, 2017, **139**, 229–243.
52 R. I. R. Ibañez, R. J. F. C. Do Amaral, R. L. Reis, A. P. Marques, C. M. Murphy and F. J. O'Brien, *Polymers*, 2021, **13**, 2510.
53 T. A. Arica, M. Guzelgulgen, A. A. Yildiz and M. M. Demir, *Mater. Sci. Eng., C*, 2021, **120**, 111720.
54 H. Holback, Y. Yeo and K. Park, *Hydrogel swelling behavior and its biomedical applications*, Woodhead Publishing Limited, 2011.
55 D. Chawla, T. Kaur, A. Joshi and N. Singh, *Int. J. Biol. Macromol.*, 2020, **144**, 560–567.
56 C. Ji, A. Khademhosseini and F. Dehghani, *Biomaterials*, 2011, **32**, 9719–9729.
57 S. D. Dutta, J. Hexiu, D. K. Patel, K. Ganguly and K. T. Lim, *Int. J. Biol. Macromol.*, 2021, **167**, 644–658.
58 S. D. Dutta, J. Bin, K. Ganguly, D. K. Patel and K. T. Lim, *RSC Adv.*, 2021, **11**, 20342–20354.
59 C. Xu, Y. Yagiz, W. Y. Hsu, A. Simonne, J. Lu and M. R. Marshall, *J. Agric. Food Chem.*, 2014, **62**, 6640–6649.
60 W. X. Du, C. W. Olsen, R. J. Avena-Bustillos, M. Friedman and T. H. McHugh, *J. Food Sci.*, 2011, **76**, M149–M155.
61 V. Platania, T. E. L. Douglas, M. K. Zubko, D. Ward, K. Pietryga and M. Chatzinikolaidou, *Mater. Sci. Eng., C*, 2021, **129**, 112412.
62 X. Chu, Y. Liu, P. Zhang, K. Li, W. Feng, B. Sun, N. Zhou and J. Shen, *J. Colloid Interface Sci.*, 2022, **608**, 1308–1322.
63 Y. Liang, B. Chen, M. Li, J. He, Z. Yin and B. Guo, *Biomacromolecules*, 2020, **21**, 1841–1852.
64 K. Nuutila, M. Samandari, Y. Endo, Y. Zhang, J. Quint, T. A. Schmidt, A. Tamayol and I. Sinha, *Bioact. Mater.*, 2022, **8**, 296–308.